



# Synthesis and characterization of rGO-supported Mo/Cu dual-doped NiO nanocomposite for the elimination of dye pollutant

Farwa Areej<sup>1</sup> · Tauseef Munawar<sup>1</sup> · Faisal Mukhtar<sup>1</sup> · Muhammad Shahid Nadeem<sup>1</sup> · Usman Ali Akbar<sup>2</sup> · Abbas Saeed Hakeem<sup>3</sup> · Faisal Iqbal<sup>1</sup>

Received: 8 November 2022 / Accepted: 30 January 2023 / Published online: 16 February 2023  
© King Abdulaziz City for Science and Technology 2023

## Abstract

Eco-friendly, highly efficient, and durable heterogeneous catalysts have gained high demand for environmental remediation caused by waste-water. Herein, NiCuMoO/rGO nanocomposite and NiCuO, NiMoO, and NiCuMoO nanoparticles were synthesized through sol–gel and ultra-sonication routes and characterized with X-ray diffraction (XRD), Fourier transform infrared spectroscopy (FTIR), Raman, UV–visible spectroscopy, Scanning electron microscopy (SEM) and energy dispersive X-ray spectroscopy (EDX). Cu and Mo doping efficiently reduced the bandgap (2.93 eV), while NiCuMoO/rGO revealed a minimum energy bandgap (2.65 eV) with spherical particles lying on rGO. The synthesized materials were tested for photodecomposition against MB dye in sun light exposure. The highest photodecomposition rate (99.2%) was attained for NiCuMoO/rGO photocatalyst. The boosted photodecomposition performance originated from the synergetic interaction of NiCuMoO and rGO that suppressed the recombination of e<sup>-</sup>/h<sup>+</sup> pairs and increased the charge carrier transfer capability. From the scavenger test, IPA and BQ have suppressed 55.0% and 45.0% MB dye, indicating that HO\* and O<sub>2</sub><sup>\*-</sup> are the dominant radicals for photocatalytic reaction. Furthermore, the structure was interrupted after 6<sup>th</sup> cycle reuse. The destruction pathway of MB using NiCuMoO/rGO photocatalyst is high, proposed large-scale utilization for the destruction of toxins.

**Keywords** Sunlight-driven photocatalyst · Toxic pollutants · Energy bandgap · Recombination · Charge carrier separation

## Introduction

Worldwide environmental and energy issues pose serious threats to living organisms (Qi et al. 2017). These issues are arising because of the rapidly growing urbanization and industrialization. Rapid industrial growth produces lethal contaminants, producing wastewater dangerous to all living organisms (Yaseen and Scholz 2019; Noreen et al. 2021). Organic dyes are among the most common forms of water pollutants. Industrial operations, including textile printing,

chemical additives, and painting, produce massive amounts of wastewater discharge annually (Al-Tohamy et al. 2022). Approximately 0.7 million tons of dyes are made annually, according to a literature survey (Zaharia and Suteu 2016). Methylene blue (MB) is among the most utilized chemicals in the dye industries (Ehrampoush et al. 2010). For the purification of contaminated water, many technologies such as microbial degradation, adsorption, coagulation, membrane process, and advanced oxidation processes have been extensively used (Zaharia et al. 2009). Recent research has focused on photocatalytic activity to remove various contaminants from wastewater (You et al. 2019). Photocatalysis can be carried out in environmental conditions where atmospheric oxygen is adequately used as an oxidant, and the complete mineralization of water occurs, maximum sunlight used, cost effective, eco-friendly and nontoxic approach (Dalrymple et al. 2010; Takanabe 2017).

Up to now, metal oxides have been attractive materials as photocatalysts for environmental remediation due to their flexible properties, various oxidation states, stability, non-toxic nature, and controlled band gap tuning, especially

✉ Faisal Iqbal  
faisal.iqbal@iub.edu.pk

<sup>1</sup> Institute of Physics, The Islamia University of Bahawalpur, Bahawalpur 63100, Pakistan

<sup>2</sup> Department of Mechanical Engineering, King Fahd University of Petroleum and Minerals, Dhahran 31261, Saudi Arabia

<sup>3</sup> Interdisciplinary Research Center for Hydrogen and Energy Storage, King Fahd University of Petroleum and Minerals, Dhahran 31261, Saudi Arabia

transition metal oxides (TMO) have attained great interest due to excellent physical and photocatalytic features (Theerthagiri et al. 2018; Ajeesha et al. 2021; Ata et al. 2021; Bibi et al. 2021; Ghafoor et al. 2021; Hannachi et al. 2022a, b). They are the perfect choice for effective photocatalytic dye degradation due to their fascinating qualities, which include their exquisite morphology, wide availability, adaptable surface composition, and exceptional mechanical, thermal, and optical capabilities (Gusain et al. 2019; Gautam et al. 2020; Parashar et al. 2020). The advancements and implications for the photocatalytic degradation of dyes are highlighted in an analysis of a wide variety of TMO with carbon composites (Yang and Wang 2018; Zhang and Jaroniec 2018). Some transition metals are copper, molybdenum, iron, cobalt, zinc, nickel, etc. Among all, NiO is a wide band gap (3.6–4 eV) material, being inexpensive, has good photostability, higher photosensitivity, exceptional stability, and low cost, which makes it attractive material used in numerous technological fields, including environmental remediation, energy, and biomedical applications (Shkir et al. 2021). Pure NiO has limited photodecomposition efficiency despite its chemical stability and suitable band edge placements due to poor optical response (Bashir et al. 2021). Due to the wider band gap, NiO response is specified in the UV region (Kannan et al. 2021). For maximum sunlight response and enhanced photoactivity of NiO, numerous modifications, including surface modification, heterogeneous composition, and element doping, have been suggested (Taeño et al. 2021; Singh et al. 2022). Among all, doping is a viable route to amend the electronic behavior of NiO because it can expand solar absorption capacity in the visible region by decreasing band gap, creating mid-energy states, and creating oxygen vacancies for optimized photocatalysis (Khatri and Rana 2020; Shakil et al. 2022). Doping of metal ions can minimize the electron–hole ( $e^-/h^+$ ) recombination process and expand light absorption capacity, which increases photocatalytic performance by creating very influential hydroxyl radicals ( $\text{OH}^*$ ) and super-oxide anion ( $\text{O}_2^{*-}$ ) as active species for photocatalysis (Ahuja et al. 2018; Lakshmana Reddy et al. 2018; Abbas et al. 2020). Many researchers worked on rare-earth-based materials; for instance, Ranjit S. Kate et al. (Kate et al. 2019) used spray pyrolysis to investigate the influence of co-doping on the structural and optical characteristics of nickel oxide (NiO) thin films. Khatri et al. (2020) reported Fe in NiO synthesized through precipitation, found the red shift in the band gap, and enhanced the photodecomposition efficiency of RB and MB dye. Varunkumar et al. (2017) synthesized Cu-doped NiO through a wet chemical route and found that morphological, optical, and structural features were improved through Cu doping.

In addition, reduced graphene oxide (rGO) is a form of graphene oxide with oxygen content reduced through chemical, thermal, and other strategies (Kavitha 2022). rGO is

a thin sheet of carbon that acts as an electron donor, co-catalyst, and electron acceptor (Agarwal and Zetterlund 2021) and acts as a channel for the transfer of an electron, thereby decreasing charge carriers' recombination rate. Several research studies demonstrated that rGO composites have higher reactivity than purely inorganic compounds with wide applications (Slimani and Hannachi 2021). Several scientists have recently worked on rGO-based materials (Yasin et al. 2020a, b; Tabish et al. 2021). For instance, using a probe sonication-aided solvothermal technique, Kadavath Santhosh et al. studied a simple and low-cost technique for manufacturing the ternary photocatalyst rGO/NiO/TiO<sub>2</sub> through three-dimensional hierarchical porous TiO<sub>2</sub> particles (Santhosh et al. 2021).

The literature survey shows the co-doping of low band gap metal in the base material and the fabrication of carbon-based material to modify the optical band gap and the material's structure for photo-decomposition. As Molybdenum oxide is promising material p-type visible light active material (Bekena et al. 2020) with a band gap of 3.85 eV and has attractive chemical and physical properties as a photocatalyst (Hakimyfarid et al. 2022) and plays an essential role in industrial and biological application owing to its exceptional redox reaction capability, unique electronic structure, structural and chemical stability and significant potential as catalyst I for use in visible as well as UV region (Bashir et al. 2022). However, shallow donor level MoO (0.59 Å) below CB introduces perturbation, and that shallowness and 4d non-localized orbital energy as compared to 3d level enhance the charge carrier's mobility when used as a catalyst (Pirzada et al. 2018). So by taking motivation from literature, ultra-sonication and co-precipitation procedures were employed to synthesize single and co-doped NiCuO, NiMoO, NiCuMoO, and rGO integrated NiCuMoO (NiCuMoO/rGO) nanocomposite, and this is 1<sup>st</sup> novel nanostructure for enhanced photodegradation.

XRD, FTIR, Raman, UV–Vis, and SEM, along with EDX, have all been used to analyze the as-synthesized samples. For the photodecomposition test, MB dye is utilized as a common toxin. In addition, recyclability and trapping experiments were conducted to evaluate the catalyst's recycling rate and the function of the main active radicals during the photocatalytic process. A mechanism for the photodecomposition of dyes is also presented.

## Experimental

### Materials

Nickel nitrate [ $\text{Ni}((\text{NO}_3)_2)$ ], molybdenum nitrate [ $\text{Mo}(\text{NO}_3)_2$ ], copper nitrate [ $\text{Cu}(\text{NO}_3)_2$ ], sodium hydroxide (NaOH), sulfuric acid ( $\text{H}_2\text{SO}_4$ ), graphite powder, potassium

permanganate ( $\text{KMnO}_4$ ), sodium nitrate ( $\text{NaNO}_3$ ), ethanol and distilled water were employed in the synthesis. All the compounds listed above are from Sigma-Aldrich and were used without further purification.

### Synthesis of NiCuMoO

NiCuMoO was synthesized using the sol–gel process. Ni, Cu, and Mo salts were used at suitable weight having 0.1 M molarity. Nickel nitrate [ $\text{Ni}(\text{NO}_3)_2$ ] is used as a base material, whereas copper nitrate [ $\text{Cu}(\text{NO}_3)_2$ ] and molybdenum nitrate [ $\text{Mo}(\text{NO}_3)_2$ ] were used as dopants. To begin synthesis, nickel nitrate [ $\text{Ni}(\text{NO}_3)_2$ ] was dissolved entirely in distilled water after being stirred continually for 30 min. The dopants salts, copper nitrate [ $\text{Cu}(\text{NO}_3)_2$ ], and molybdenum nitrate [ $\text{Mo}(\text{NO}_3)_2$ ] were then dissolved in the base solution and mixed for 1 h. After that, sodium hydroxide (NaOH) solution (0.1 M) was added dropwise to achieve a basic solution (pH=9). To create precipitates, the combined solution was stirred for 3 h. It was then washed with ethanol and water, filtered, then dried at 80° C for 6 h before being annealed at 700° C. All other compositions were prepared using a similar procedure.

### Synthesis of NiCuMoO/rGO

As mentioned in literature (Munawar et al. 2020a, b) graphene oxide (GO) was initially prepared using the Hummers process. In this experiment, a sufficient amount of  $\text{NaNO}_3$  and graphite powder was poured into a beaker, concentrated  $\text{H}_2\text{SO}_4$  was injected, and the mixture was agitated for 1 h. After removing the ice bath and adding  $\text{KMnO}_4$ , the mixture was stirred for 48 h.  $\text{H}_2\text{O}_2$  and hot water were added laterally, and  $\text{H}_2\text{SO}_4$  was utilized to remove  $\text{KMnO}_4$ . After that, distilled water is used for washing to achieve a neutral pH level for the production of graphene oxide suspension. Finally, reduced graphene oxide (rGO) was created by lowering GO with reducing agents (hydrazine and ammonia). NiCuMoO/rGO was made by dispersing a ratio of 1:1 (rGO and NiCuMoO) in 100 mL of distilled water. Afterward, the combined solution was ultrasonicated for half an hour and then dried for 1 h at 60 °C to obtain a black color powder.

### Photocatalytic test

The photocatalytic performance of all prepared catalysts was investigated under solar irradiation by examining MB photodegradation. Initially, 20 mg of NiCuO, NiMoO, NiCuMoO, and NiCuMoO/rGO catalyst was dispersed in 50 mL dye (5 ppm). First, the suspensions were stirred under the dark for 80 min to achieve adsorption–desorption equilibrium, then exposed to solar irradiation. UV–Vis spectra measured light absorption by catalyst and dye concentration after

exposure. The degradation efficiency (%) of corresponding pollutants was intended by using relation (A et al. 2020):

$$\eta = ((C_0 - C_t)/C_0) \times 100 \quad (1)$$

Here,  $C_0$  and  $C_t$  are the initial and final concentrations of dyes before and after sunlight exposure. Moreover, trapping experiments are performed to investigate the mechanism of the photodegradation reaction. Here, EDTA-2Na for  $h^+$ , ASC for  $O_2^{*-}$ ,  $\text{AgNO}_3$  for  $e^-$ , and IPA for  $HO^*$  scavengers were used. To assess the stability, a repeated photodegradation test was executed 6 times.

### Characterization

A powder X-ray diffractometer (XRD: Bruker D8 advance laboratory diffractometer) with  $CuK\alpha$  radiation ( $\lambda=1.5406 \text{ \AA}$ ) in the range of  $2\theta=35^\circ-85^\circ$  was used to examine the structural analysis. Raman (confocal Micro-Raman, 0–2500  $\text{cm}^{-1}$ ) and FTIR spectra were used to identify the molecular structure and chemical bonding (400–4000  $\text{cm}^{-1}$ ). A UV visible spectrophotometer was utilized at ambient temperature in the wavelength range of 250–800 nm for optical evaluation. SEM operated at 20.0 kV of the model (Emcrafts cube 2020) was used to expose surface morphology and elemental confirmation through built-in EDX.

## Results and discussion

### XRD

A material's crystal structure and phase composition can be determined through XRD analysis. At room temperature, the synthesized samples were structurally examined by X-ray diffraction technique (range of  $2\theta=35^\circ-85^\circ$ ). The XRD patterns of NiCuO, NiMoO, NiCuMoO, and NiCuMoO/rGO are shown in Fig. 1. All diffraction patterns of as-synthesized samples are in strong agreement with the JCPDS No.01–075–0269 (NiO). No secondary peak appeared, which indicates that the grown samples are highly crystalline. The slight shift in peaks of doped samples originated from ionic radii differences of host lattice  $\text{Ni}^{+2}$  (0.69  $\text{\AA}$ ) and dopant atoms  $\text{Cu}^{+2}$  (0.73  $\text{\AA}$ ),  $\text{Mo}^{+2}$  (0.65  $\text{\AA}$ ), (Fig. 2a). The incorporation of higher radii Cu dopant shifts diffraction angle  $2\theta$  towards the lower end, increasing volume 73.297  $\text{\AA}^3$ , while smaller radii element Mo shifts the XRD diffraction outcome toward ascending  $2\theta$ , and volume decrease 72.8196  $\text{\AA}^3$  (Table 1). While for Cu and Mo doped NiCuMoO and NiCuMoO/rGO samples, the estimated volume is 73.079  $\text{\AA}^3$  and 73.117  $\text{\AA}^3$ , with various lattice constants showing their influence in NiO lattice. Table 1 shows the estimated

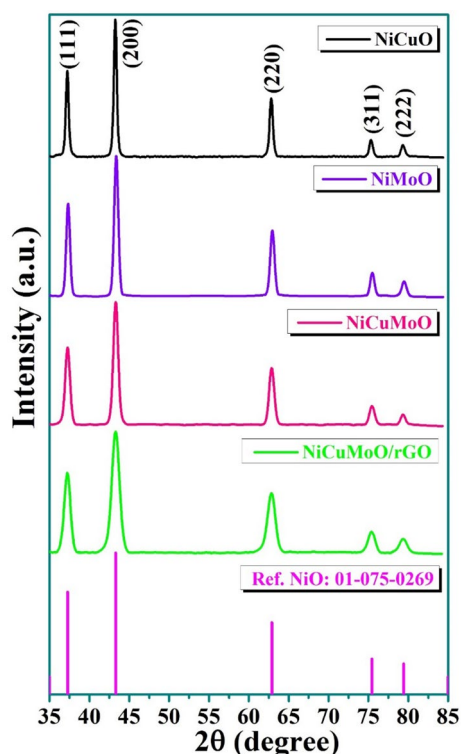


**Fig. 1** a XRD profile for all NiO-based materials

structural data, such as lattice constants, bond length, and spacing. The typical growth orientation of synthesized materials could be accessed through texture coefficient ( $TC_{(hkl)}$ ), evaluated from the given relation (Shiri et al. 2019):

$$TC_{(hkl)} = \frac{I_{(hkl)}/I_{o(hkl)}}{\left(\frac{1}{N}\right)I_{(hkl)}/I_{o(hkl)}} \quad (2)$$

$I_{(hkl)}$  = XRD computed intensity,  $I_{o(hkl)}$  = standard plane intensity, and  $N$  = the number of peaks. Generally, it is recommended that  $TC_{(hkl)} > 1$  gives good crystal development. Here, in Fig. 2b, the  $TC_{(hkl)}$  values for NiCuO against (200), (220) plane, for NiMoO against (220) plane, for NiCuMoO against (200), (220) plane, for NiCuMoO/rGO for (220) plane are  $> 1$ , which validates their good growth.

The crystallite size ( $D$ ) obtained from several methods that differed from each other but showed the same tendency (Table 2) were employed. These calculations were carried out using techniques of previous reports (Munawar et al. 2020c). Figure 2c, e depicted the Scherrer, W–H, and SSP plots. Accordingly, all results revealed that  $D$  lies in the nano range. Further, SSP results are more reliable because this route utilizes the maximum data points for fitting. The decreasing trend in  $D$  values was observed for NiCuO, NiMoO, NiCuMoO, and NiCuMoO/rGO samples, indicating

the fluctuation in lattice disruption through doping and rGO integration. Other interesting results show that strain  $\epsilon$  values are negative, meaning the compressive stress for all catalysts. The variation of dislocation density ( $\delta = 1/D^2$ ) increases for NiCuO, NiMoO, NiCuMoO, and NiCuMoO/rGO samples, respectively, NiCuMoO/rGO having  $\delta$  value  $4.089 \text{ nm}^{-2}$  suitable for dye adsorption. Table 2 illustrates the  $D$ ,  $\epsilon$ , and dislocation density ( $\delta = 1/D^2$ ).

## FTIR

FTIR spectroscopy was executed within ( $400\text{--}4000 \text{ cm}^{-1}$ ) range to determine the presence of functional groups in the catalyst. It also determines grown materials' chemical bond interaction and vibrational positions. Figure 3a depicts the recorded FTIR spectra for NiCuO, NiMoO, NiCuMoO, and NiCuMoO/rGO nanocomposites. The typical interaction of oxygen and metal bonds lies in  $400\text{--}600 \text{ cm}^{-1}$  in all samples. For NiCuO, the peak in the FTIR spectrum appears approximately at  $423$  and  $478 \text{ cm}^{-1}$ , Ni–O bonding in bending modes is responsible for the high absorption band appearing at  $423 \text{ cm}^{-1}$ . At the same time, Cu–O stretching indicates a high absorption band observed at  $478 \text{ cm}^{-1}$  (Papadimitropoulos et al. 2006; Ramya et al. 2016; Bodade et al. 2017). The broadness of the peak evidences the crystalline structure of the nickel oxide catalyst. For the sample, NiMoO peaks appeared at  $424$  and  $479 \text{ cm}^{-1}$ . These bands are caused by the vibrational modes of Mo–O–Mo and Ni–O–Mo (Tadjarodi et al. 2014). The peak at  $417$ ,  $457$ , and  $510 \text{ cm}^{-1}$  for sample NiCuMoO is due to the copper molybdate crystalline phase's vibrational mode. Lastly, for sample NiCuMoO/rGO, peaks that appeared at  $416$ ,  $456$ , and  $590 \text{ cm}^{-1}$  originate from metal oxygen interaction, and  $1541 \text{ cm}^{-1}$  in broad range ( $1460\text{--}1575 \text{ cm}^{-1}$ ) arise from C=O stretching. Minor band variations appear to imply an interaction between rGO and NiCuMoO. These observations support that rGO is integrated with NiCuMoO sample. Thus, NiCuMoO/rGO nanocomposite is formed (Lingaraju et al. 2019).

## Raman analysis

Raman spectroscopy is useful for assessing dopant incorporation, imperfections, oxygen vacancies, and disorder within host material (Belkhaoui et al. 2019). As a result, all synthesized samples were subjected to Raman analysis to uncover imperfections and disorders in the material. Figure 3b shows the Raman spectra for all samples. Nickel corresponds to the cubic group with Fd-3 m space group and has two sorts of sublattices (tetrahedral and octahedral surroundings). Td & D3d are tetrahedral (T) and octahedral (O) sublattices for cubic structure, respectively (Dharmaraj et al. 2006). As per group theory research, just five optical modes ( $A_{1g} + E_g + 3T_{2g}$ ) of the pure cubic structure are

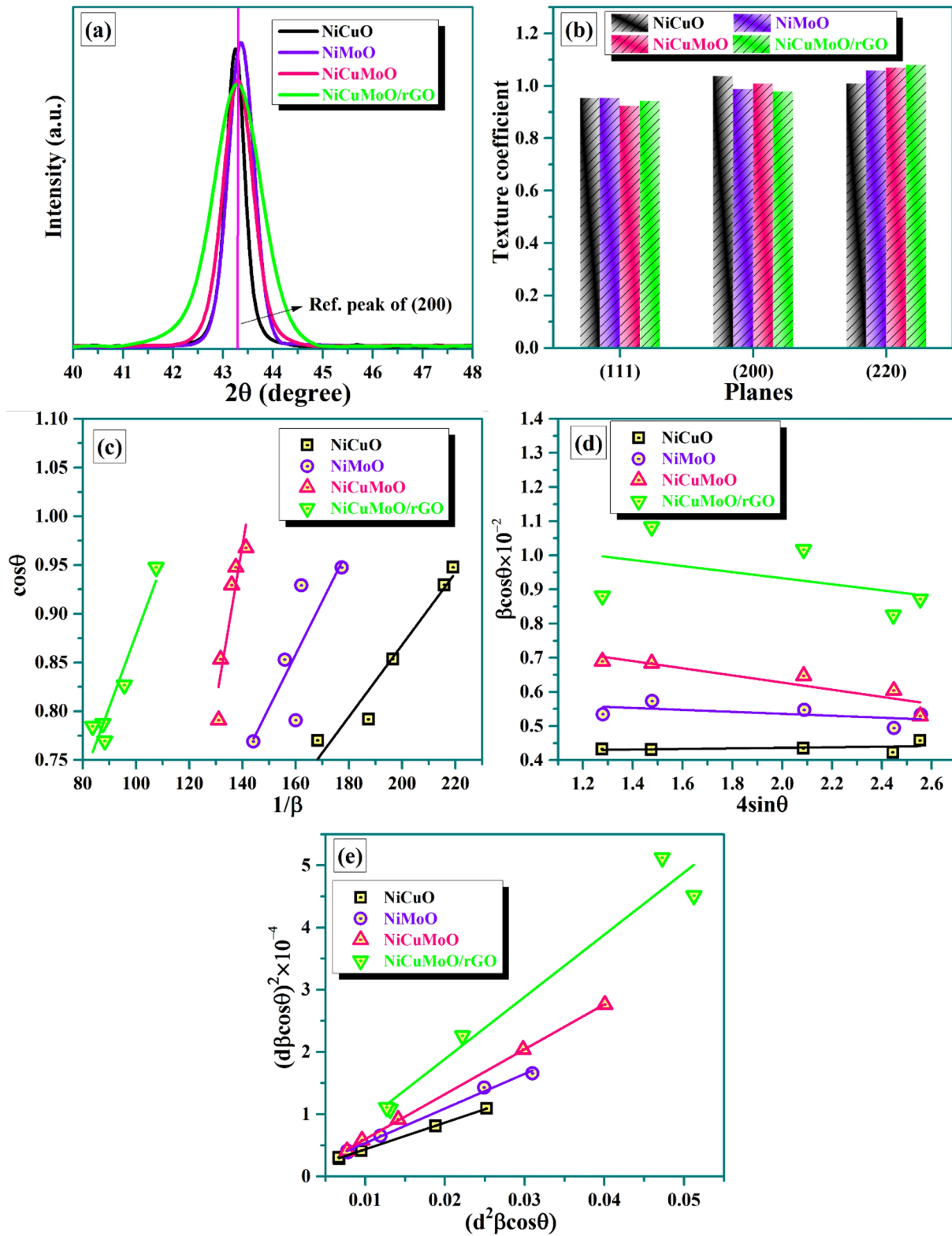


Fig. 2 a XRD peak shifting, b Texture coefficient, c Scherrer plots, d W–H plots, and e SSP plots for all NiO-based materials

**Table 1** The structural parameters of as-prepared materials

| Samples     | $a=b=c$ (Å) | Volume Å <sup>3</sup> | Density (g/cm <sup>3</sup> ) | Bond-length (nm) | $d$ -spacing |
|-------------|-------------|-----------------------|------------------------------|------------------|--------------|
| NiCuO       | 4.185       | 73.297                | 6.7668                       | 2.093            | 1.6901       |
| NiMoO       | 4.176       | 72.819                | 6.8113                       | 2.088            | 1.6863       |
| NiCuMoO     | 4.181       | 73.079                | 6.7871                       | 2.09             | 1.6884       |
| NiCuMoO/rGO | 4.182       | 73.117                | 6.7835                       | 2.091            | 1.6886       |

**Table 2** Geometric parameters of as-prepared materials

| Samples     | Average crystallite size (nm) |               |     |     | Lattice strain $\epsilon \times 10^{-4} \times 10^{-3}$ |       | Dislocation density $\delta \times 10^{-3}$ (nm <sup>-2</sup> ) |
|-------------|-------------------------------|---------------|-----|-----|---|-------|---|
|             | Scherrer                      | Scherrer plot | W–H | SSP | W–H   | SSP   |   |
| NiCuO       | 33                            | 39            | 35  | 34  | 0.847   | 1.586 | 0.904   |
| NiMoO       | 27                            | 26            | 24  | 26  | -2.86   | -2.91 | 1.366   |
| NiCuMoO     | 23                            | 24            | 27  | 20  | -10.5   | -7.01 | 1.860   |
| NiCuMoO/rGO | 16                            | 21            | 13  | 14  | -8.88   | -6.67 | 4.089   |

important Raman modes that emerge owing to the movement of atoms and oxygen ions (Chandekar et al. 2021). Raman modes under 600 cm<sup>-1</sup> belong to octahedral sites, while active modes exceeding 600 cm<sup>-1</sup> refer to tetrahedral sites (Ghosh et al. 2021). Raman peak was detected at 501 cm<sup>-1</sup> for the NiCuO sample, and the prominent peak may see the occurrence of 1LO vibrational mode at 501 cm<sup>-1</sup> (Patel et al. 2017; Gawali 2020). However, when active Cu<sup>2+</sup> ions are present in the octahedral sites, the cubic symmetry of the octahedral sites (Fd-3 m) is converted into tetrahedral symmetry, causing minimal deformation in such sublattice sites. Peaks observed at 507 cm<sup>-1</sup> for NiMoO material can correlate to the symmetric and anti-symmetric vibration modes (A<sub>g</sub> and B<sub>g</sub>) associated with Mo=O and symmetrical stretch mode (A<sub>g</sub>) of Mo–O–Ni (Alemán-Vázquez et al. 2005; Sone et al. 2016). Because of the dual doping, NiCuMoO has peaked at 513 cm<sup>-1</sup> and 457 cm<sup>-1</sup> with varying intensities. Finally, NiCuMoO/rGO has 467, 514, and 1379 cm<sup>-1</sup>, with the 1379 cm<sup>-1</sup> peak attributable to the existence of rGO, which belongs to the D band of GO sheets (Marinoiu et al. 2020). The symmetry can be because the D band emanates from the edges. At 1379 cm<sup>-1</sup> strong peak developed (D band, related to the existence of structural defects) (Iqbal et al. 2020). As a result, Raman analysis reveals the existence of a significant proportion of defects in the material, which is beneficial for photocatalysis (Maniammal et al. 2018).

### UV–Vis study

The material's optical properties, such as energy bandgap, could be estimated through a UV–Vis study. Figure 3c reveals the optical absorbance spectra for NiCuO, NiMoO, NiCuMoO, and NiCuMoO/rGO nanocomposite. For NiO,

which lies below 380 nm (UV spectra) and is not applicable in wide sunlight spectra. When dopants are added, the absorption shifts significantly in a larger wavelength, enhancing sunlight-capturing ability. The recorded redshift through doping results in absorption is observed at 390, 395, and 413 nm for Cu, Mo, and dual doped (Cu, Mo) samples, respectively. For NiCuMoO/rGO nanocomposite, the optical response is a collection of the electronic grouping of  $\pi$ -systems and numerous rGO rings, which respond excellently to solar light. The absorbance at 423 nm was observed in NiCuMoO/rGO nanocomposite, which covered the maximum solar light among all catalysts. In Fig. 3d, the recorded transmittance spectra indicate that NiCuO, NiMoO, NiCuMoO, and NiCuMoO/rGO nanocomposite are good transmitters in longer wavelength regions. The optical band gap ( $E_g$ ) was estimated using the traditional Tauc's method [ $ah\nu = A(h\nu - E_g)^n$ ] (Brijesh and Nagaraja 2019). To calculate the energy bandgap, the plot of  $h\nu$  on the  $x$ -axis and  $(ah\nu)^2$  on the  $y$ -axis was drawn and extrapolate the curve to touch at the  $x$ -axis. The decrement in  $E_g$  values 3.34, 3.23, 2.93 eV, for singular Cu, Mo doped, dual doped (Cu, Mo) and 2.65 eV for NiCuMoO/rGO nanocomposite, respectively, were observed and given in (Fig. 3e). This decrement might be linked to crystal size variation, strong orbital coupling, and generated defects. The incorporation of rGO can facilitate the transfer of e<sup>-</sup> into rGO and create maximum defects favorable for capturing greater sunlight.

### Morphology and elemental analysis

SEM analysis of NiCuO, NiMoO, NiCuMoO, and NiCuMoO/rGO samples was done to evaluate the surface features of catalysts. In Fig. 4, SEM images in different resolution scales are presented. Figure 4a–a3 reveals irregular

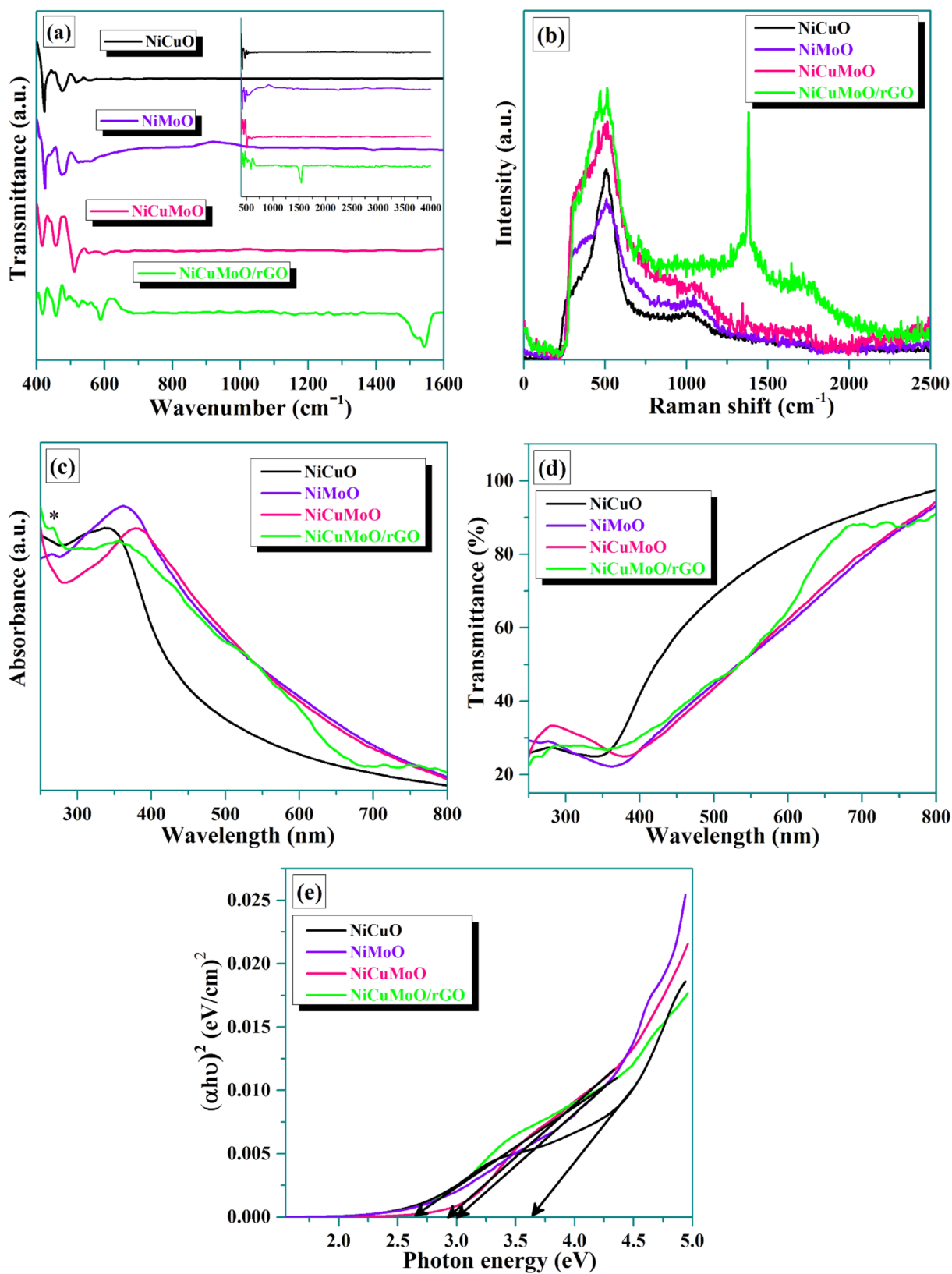


**Fig. 3** a FTIR spectra, b Raman spectra, c UV-Vis absorption spectra, d UV-Vis transmittance spectra, and e Tauc's plots for all NiO-based materials

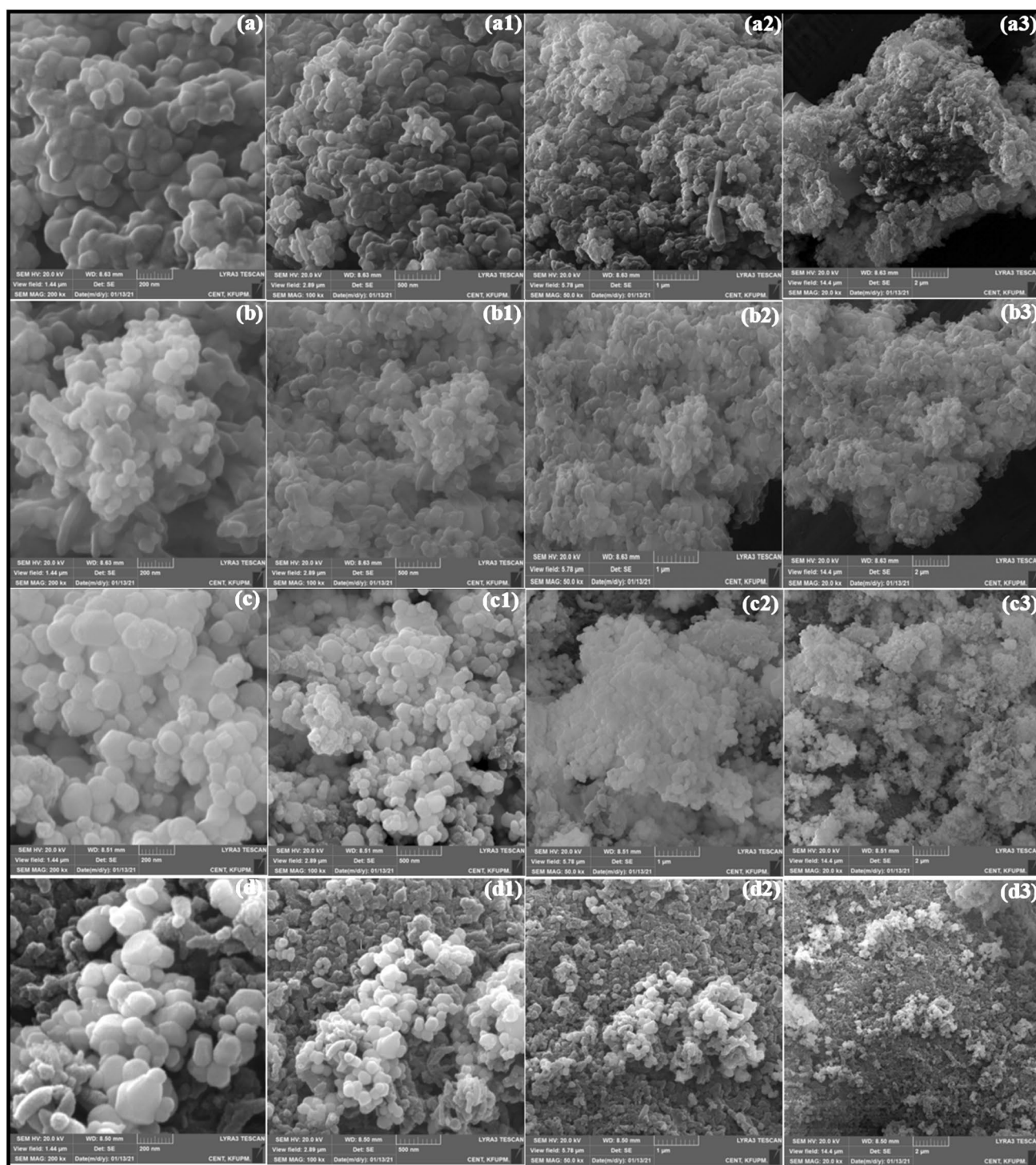


**Fig. 4** SEM images at different resolutions **a–a3** NiCuO, **b–b3** NiMoO, **c–c3** NiCuMoO, and **d–d3** NiCuMoO/rGO

NiCuO particles that stick together. The synthesized NiMoO (Fig. 4b–b3) nanoparticles have spherical morphology; however, the introduction of Mo has suppressed the agglomeration. Well-shaped particles with a spherical pattern were observed when Cu and Mo were injected in NiO

(Fig. 4c–c3). Figure 4d–d3 shows SEM images of NiCuMoO/rGO nanocomposite, where NiCuMoO particles are distributed over rGO. The mutual binding of NiCuMoO and rGO reduced the particle size, which fits well with XRD data. This shape harvest more photons from the solar



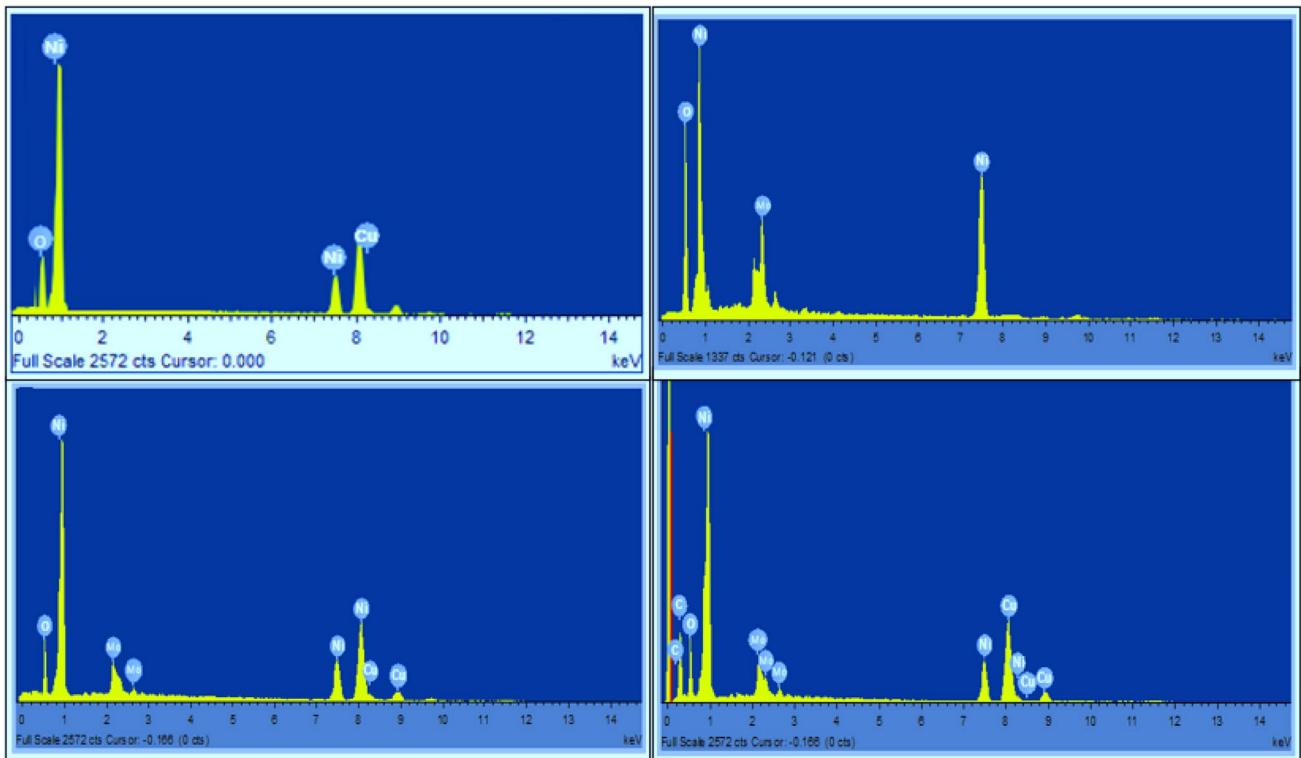


**Fig. 5** EDX spectra of NiCuO, NiMoO, NiCuMoO, and NiCuMoO/rGO, along with elemental composition

spectrum and rapid transfer of electron among the NiCu-MoO and blackish rGO that actively participate in the destruction of dyes as rGO accept electron and convert them into superoxide anion that attacks pollutant dyes molecules and degrade them into harmless product. Figure 5 shows the maximum peaks of Ni, Cu, and O in NiCuO, Ni, Mo, O in NiMoO, Ni, Cu, Mo, O in NiCuMoO, and C, Ni, Cu, Mo, O in NiCuMoO/rGO nanocomposite EDX patterns, respectively. The required elements in synthesized products confirm that all samples are well prepared (Table 3).

**Photocatalytic activity**

The photocatalytic degradation ability of as-prepared samples is evaluated against MB dye solution under sunlight illumination after attaining adsorption–desorption

equilibrium in the dark. MB has a distinctive dark blue color when oxidized and is transparent when reduced (Jiao et al. 2015). For the removal of ecologically toxic substances, the photocatalytic degradation experiment of MB dye was performed for all synthesized NiCuO, NiMoO, NiCuMoO, and NiCuMoO/rGO nanocomposite samples, and the breakdown of MB dye was carefully studied using UV–Visible spectroscopy. Figure 6a–d represents the photocatalytic decolorization of MB dye in the presence and absence of a catalyst. Fast photocatalytic efficiency for 80 min was observed, followed by a reduction in color. The intensity of the MB absorbance peak decreased steadily for NiCuO, NiMoO, and NiCuMoO samples. At the same time, it was faster for NiCuMoO/rGO nanocomposite, and overall photodegradation was completed under solar illumination after 80 min as per the analysis. However, a minimal breakdown

**Table 3** Elemental compositions obtained from EDX analysis

| Elements | NiCuO   |         | NiMoO   |         | NiCuMoO |         | NiCuMoO/rGO |         |
|----------|---------|---------|---------|---------|---------|---------|-------------|---------|
|          | Weight% | Atomic% | Weight% | Atomic% | Weight% | Atomic% | Weight%     | Atomic% |
| O        | 35      | 66.65   | 35      | 68.17   | 32      | 65.17   | 24          | 34.76   |
| Ni       | 55      | 28.55   | 52      | 27.61   | 48      | 26.65   | 21          | 8.29    |
| Cu       | 10      | 4.80    | 0.00    | 0.00    | 8       | 4.10    | 12          | 4.37    |
| Mo       | 0.00    | 0.00    | 13      | 4.22    | 12      | 4.08    | 18          | 4.35    |
| C        | 0.00    | 0.00    | 0.00    | 0.00    | 0.00    | 0.00    | 25          | 48.73   |
| Total    | 100     | 100     | 100     | 100     | 100     | 100     | 100         | 100     |

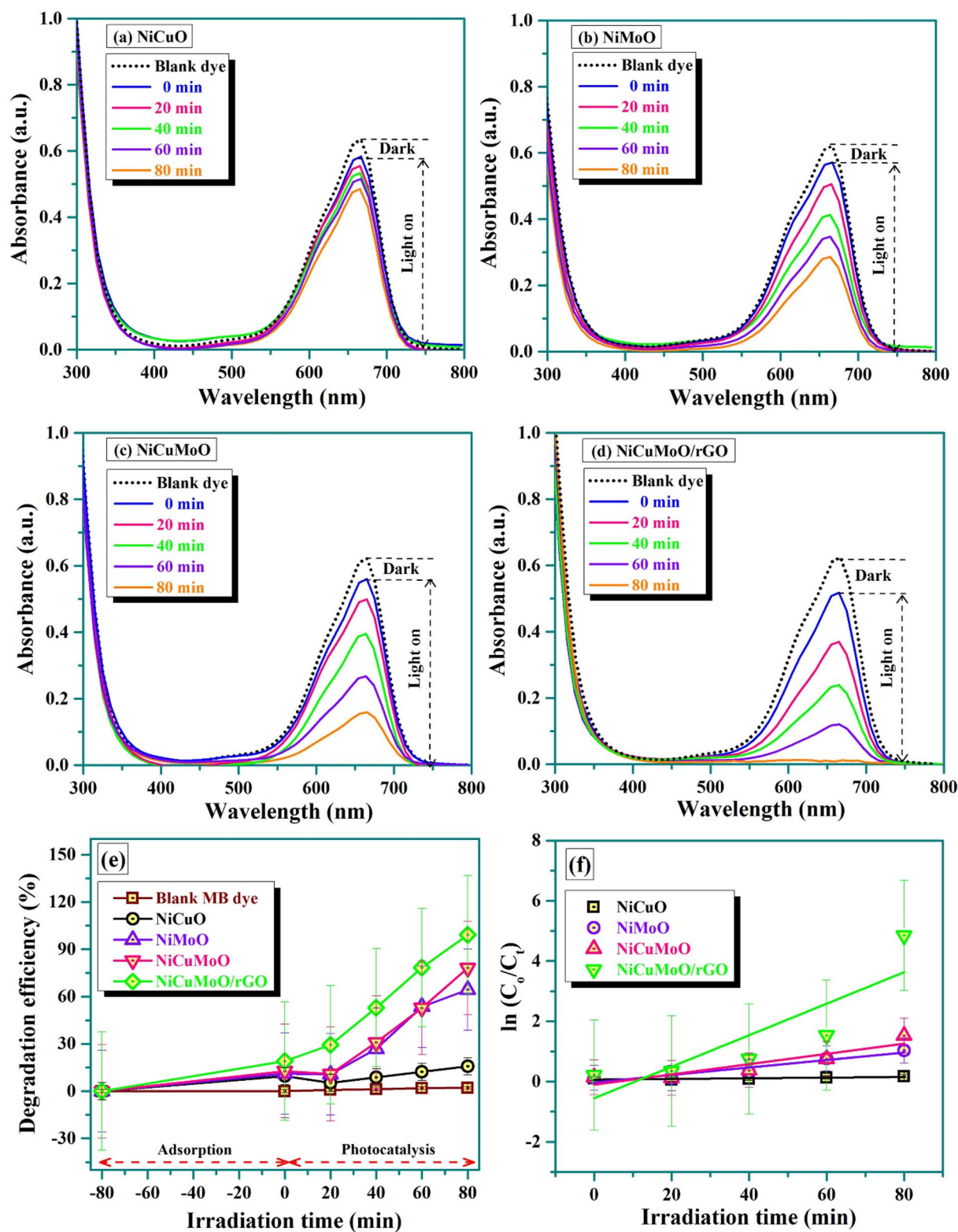


**Fig. 6** Absorption spectra of MB after treating with grown catalysts **a** NiCuO, **b** NiMoO, **c** NiCuMoO, **d** NiCuMoO/rGO, **e** degradation efficiency at different times, **f** rate constant plots

was seen without introducing a catalyst, as presented in Fig. 6e. The adsorption was studied by obtaining the adsorption spectrum of blank dye and then performed after the reaction in the dark. Figure 6e depicts the adsorption percentage (9.5%, 11.1%, 12.7%, and 19%) and degrading efficiency of NiCuO, NiMoO, NiCuMoO, and NiCuMoO/rGO nanocomposite samples having 15.8%, 64.3%, 78.2%, and 99.2%, respectively. Photodegradation has a pseudo-first-order kinetic condition, as seen in Fig. 6f, and is estimated from the given relation (Oladipo 2021).

$$C_t = C_0 e^{-kt} \quad (3)$$

$$\ln(C_0/C_t) = kt \quad (4)$$

whereas  $k$  denotes the rate constant. Figure 6f shows graphs of the natural logarithm of concentration against irradiation time. For NiCuO, NiMoO, NiCuMoO, and NiCuMoO/rGO nanocomposite, the computed  $k$  values are  $0.0011 \text{ min}^{-1}$ ,  $0.01239 \text{ min}^{-1}$ ,  $0.01703 \text{ min}^{-1}$ , and  $0.0523 \text{ min}^{-1}$ , respectively. However, NiCuMoO/rGO nanocomposite catalyst has decomposed (99.2%) MB dye and has a greater rate constant value. Therefore, it is reasonable to state that NiCuMoO/rGO catalyst has greater potential to decompose various organic contaminants as per findings. The comparison of photodegradation efficiency with other reported materials is given in Table 4.

### Operating parameters

Appropriate dosage of the tested catalyst raises the production of  $e^-/h^+$  pairs, thereby, the rapid formation of ROS for exceptional photodecomposition efficiency. Hence the influence of catalyst dosage on the photodecomposition process was accessed using NiCuMoO/rGO varied from 20 to 35 mg, keeping  $\text{pH}=9$  and MB concentration at 10 ppm, respectively (Fig. 7a). As shown, the optimal photocatalyst quantity (25 mg) showed maximum photodecomposition (99.2%) towards MB, and then a decline of 97.1% happened for a higher photocatalyst amount (35 mg). For photocatalyst amounts (20–25 mg), abundant active sites were available for reaction, which creates extra radicals for the photodecomposition phenomenon. Gradual decline in efficiency was detected through additional photocatalyst amount; since aggregation of NiCuMoO/rGO particles illustrated screening effect, resulting in lower photon capturing ability of catalyst. The pH significantly affects the photodecomposition efficiency as different pollutants contain varied pH. The pH effect was observed through varying pH from 5 to 11, as shown in Fig. 7b, for NiCuMoO/rGO (25 mg), initial MB concentration (10 ppm). At a pH higher (greater than 7), the surface of NiCuMoO/rGO is negatively charged, while at lower pH (less than 7), it adapts positively charged. MB being cationic, a higher pH value is

**Table 4** Comparison of degradation efficiency of grown nanocomposite catalyst with other reported materials

| Photocatalyst  | Degradation efficiency (%) | Refs.                                |
|--|----------------------------|--------------------------------------|
| NiO-CaO  | 96.5                       | Song and Zhang (2010)                |
| Ni/NiO/TiO <sub>2</sub>                                | 98.0                       | Zhu et al. (2018)                    |
| NiO-MWCNT  | 92.4                       | Nath et al. (2021)                   |
| NiO/AgNbO <sub>3</sub>                                 | 85.0                       | Shu et al. (2010)                    |
| CuO-NiO  | 97.2                       | Senobari and Nezamzadeh-Ejhih (2018) |
| NiO-ZnO  | 65.0                       | Kanjwal et al. (2015)                |
| NiO/MgO  | 87.0                       | Fuku et al. (2018)                   |
| Ag <sub>2</sub> O-NiO/CuFe <sub>2</sub> O <sub>4</sub> | 96.7                       | Liu et al. (2020)                    |
| Cu-NiO-ZrO <sub>2</sub>                                | 99.0                       | Areeb et al. (2021)                  |
| NiO/Cr <sub>2</sub> O <sub>3</sub>                     | 93.6                       | Yadav et al. (2022)                  |
| NiCuMoO/rGO  | 99.2                       | Present                              |

favorable for MB adsorption on NiCuMoO/rGO surface; consequently, higher photodecomposition efficiency (99.2%) and 96.5% occur in basic and neutral conditions. Further higher pH value reduces photodecomposition efficiency due to electrostatically repulsion between negative photodecomposition surface and ROS involved in the redox mechanism, suppressing the efficiency. The photodecomposition study was executed by varying the initial MB concentration from 10 to 25 ppm, keeping NiCuMoO/rGO 25 mg and  $\text{pH}=9$  fixed (Fig. 7c). Results showed that photodecomposition efficiency using NiCuMoO/rGO against MB decreased from 10 to 25 ppm. The maximum observed efficiency (99.2%) against 10 ppm declines to 90.3% at 25 ppm MB concentration. Therefore, the photodecomposition could be enhanced by lowering the initial MB concentration. This occurs as more MB molecules were integrated on NiCuMoO/rGO surface by increasing the dye concentration. Since MB molecules covered numerous active sites, the adsorption was reduced, and the regeneration of radicals was hampered. Moreover, more photons were blocked from reaching the photocatalyst surface; ROS production was slowed. Furthermore, trapping experiments are performed to investigate the mechanism of the photodegradation reaction. Here, EDTA-2Na for  $h^+$ , BQ for  $O_2^{\bullet-}$ , AgNO<sub>3</sub> for  $e^-$ , and IPA for HO\* scavengers were used. Results showed that BQ and IPA were the prominent scavengers in the photoreduction process. The recorded reduced efficiencies are 99.2% (without scavenger), 88.0% (AgNO<sub>3</sub>), 82.0% (EDTA-2Na), 55.0% (IPA), and 45.0% (BQ), respectively (Fig. 7d). Hence HO\* and  $O_2^{\bullet-}$  are the dominant radicals for destructing MB dye. Furthermore, NiCuMoO/rGO nanocomposite exhibits greater recycling ability toward MB dye till the 6th cycle with just a 6% fall in photocatalytic degradation rate (Fig. 7e), demonstrating its high reusability. Figure 7f shows XRD patterns of freshly synthesized NiCuMoO/rGO catalyst after the 6th cycle, indicating that structure was interrupted after the 6th

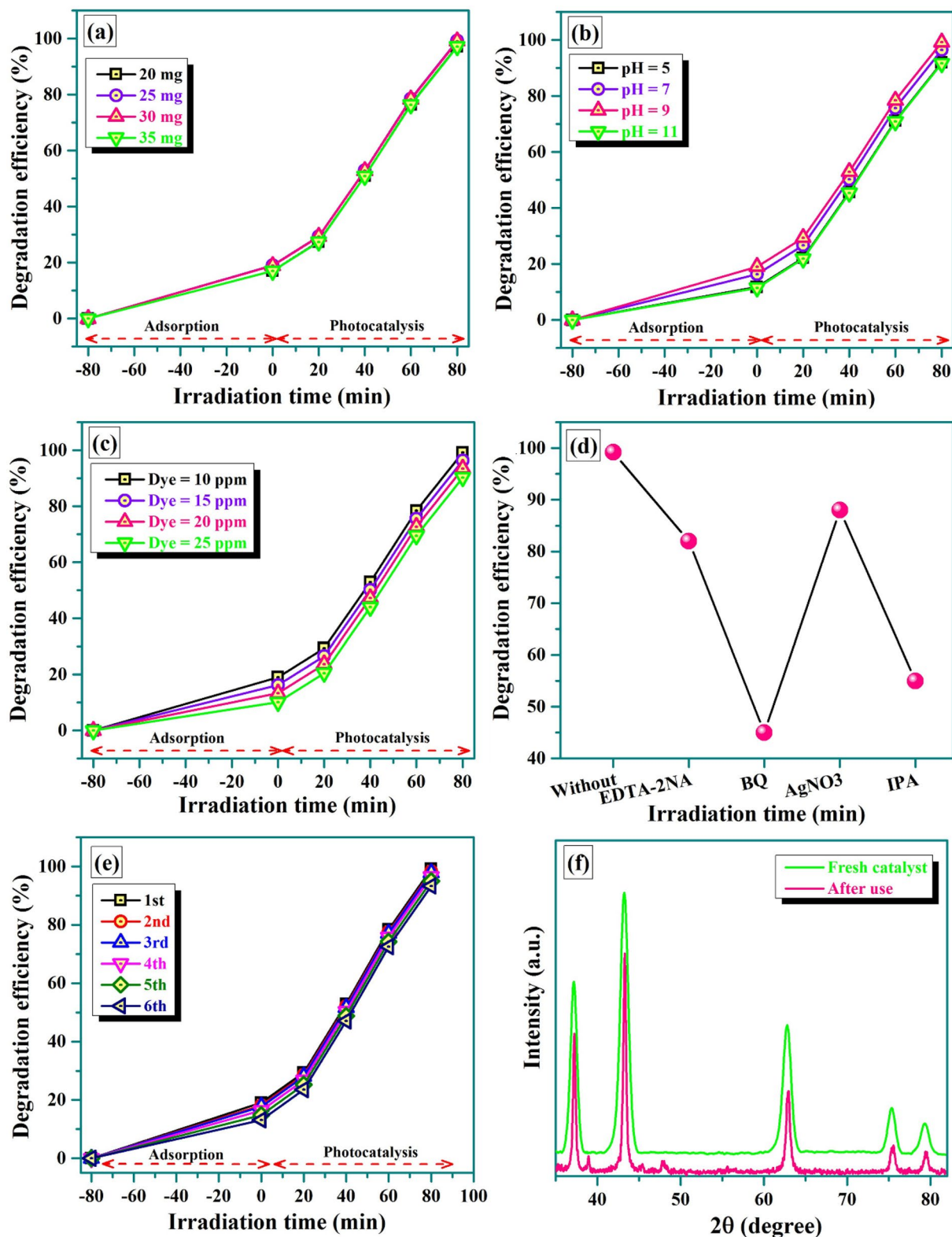


**Fig. 7** Operational parameters effect on MB degradation using NiCuMoO/rGO **a** effect of catalyst, **b** effect of pH, **c** effect of initial dye concentration, **d** scavenger effect, **e** recyclability test, and **f** again XRD pattern

cycle. This type of catalyst is highly demanded for large-scale utilization to destroy toxins.

### Photocatalytic mechanism

The formation of the  $e^-/h^+$  pairs upon sunlight irradiation, the charge carrier's separation, the transmission of photo-triggered carriers to the active site, and the creation of active oxygen species are all part of the photocatalysis process. According to UV–Vis analysis, NiCuMoO/rGO nanocomposite band gap is suitable for a photocatalytic perspective.

The band edge potentials are obtained from equation (Munawar et al. 2022).

$$E_{CB} = X - E_e - 0.5E_g \quad (5)$$

Here  $x$  = electronegativity of semiconductor, where  $E_e$  = free  $e^-$  energy,  $E_g$  = bandgap and,

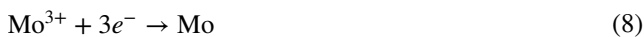
$E_{CB}$  = conduction band potential. The calculated value of  $E_{CB}$  for Ni is 0.145 eV with  $E_g$  (2.65 eV).

$$E_{VB} = E_{CB} + E_g \quad (6)$$

Similarly, from the above equation, the value of  $E_{VB}$  (valence band potential) is obtained, i.e., 2.795 eV. The photocatalysis mechanism is described as follows. The entire photocatalytic degradation can be categorized into three stages: solar light absorption through the catalysts' surface and photoexcitation of electrons to obtain holes. And finally, photochemical reactions across the catalysts' surface through the photogenerated electron–hole pairs. The degradation rate of the sample (NiCuMoO) was significantly greater than NiCuO and NiMoO, indicating that co-doping of Cu and Mo can greatly enhance NiO's photocatalytic performance. Because of the introduction of doping energy levels inside the energy band gap of NiCuMoO. The electrons within VB shift to the energy level created due to Cu doping below the CB via interconversion between  $Cu^+$  and  $Cu^{2+}$ , whereas Cu is subjected to electron trapping in the following way:

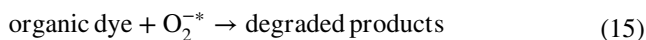
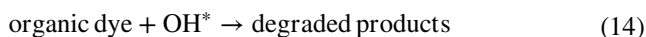
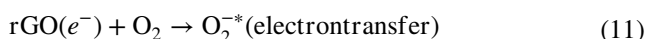
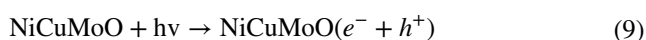


In addition, when Mo is introduced, the potential of  $Mo^{3+}/Mo$  is  $-0.2$  above from  $E_{CB}$  of NiCuMoO, with fruitless potential for redox reaction but can capture exciting  $e^-$  for effective charge separation, and this  $e^-$  can jump towards rGO sheets for effective redox reactions. Mo is thus amenable to electron trapping in the following manner:



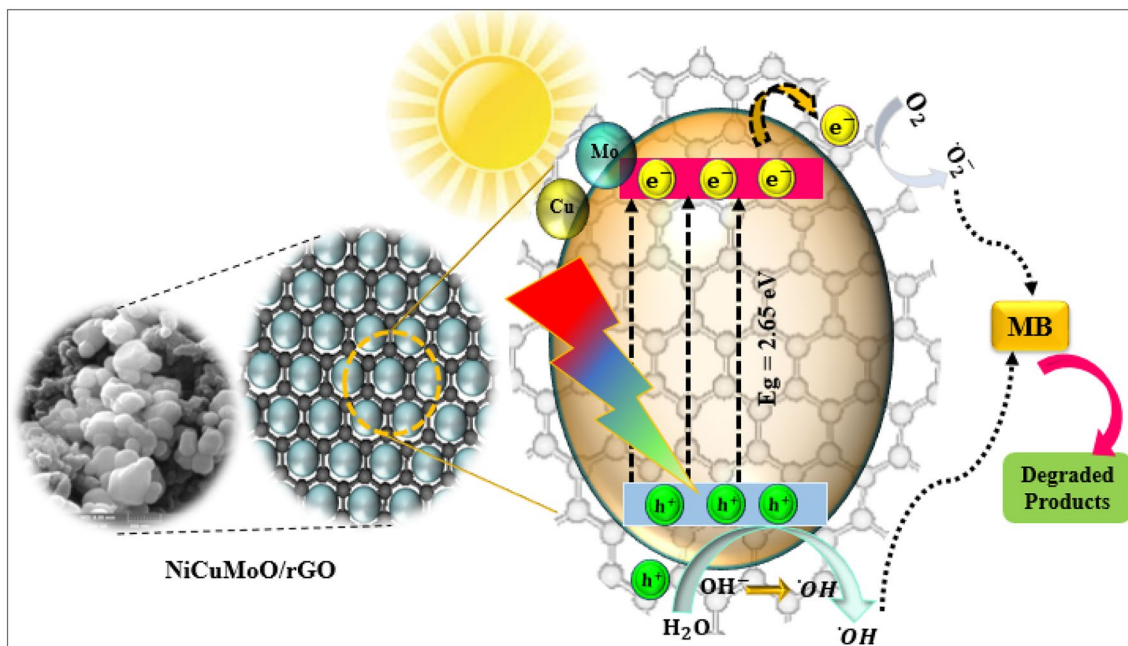
Thus, Cu and Mo co-doping may enable the photo-generated electrons to enhance  $e^-/h^+$  separation while speeding up the charge transport process, leading to improved photocatalytic performance.

In sample NiCuMoO/rGO nanocomposite, when sunlight strikes the catalyst,  $e^-/h^+$  pairs are developed. rGO is a thin sheet of carbon that could be utilized as an electron donor, co-catalyst, and electron acceptor because of its good conductivity. Because of the complex web of interlinked  $sp^2$  carbons present in reduced graphene oxide (rGO), electron mobility is impressive, preventing electron–hole recombination. Irradiation causes NiCuMoO to exhibit excellent charge carrier separation, with holes forming in the material's valence band, allowing for oxidation while electrons are confined by rGO sheets and readily available for reduction. Hence, NiCuMoO/rGO nanocomposite surpasses all other samples attributed to the following characteristics, (i) reduction in the bandgap, (ii) excellent charge separation and more defects, and (iii) expansion in surface area. The charge transportation process is illustrated in Scheme 1.



### Conclusion

In summary, NiCuMoO/rGO nanocomposite and NiCuO, NiMoO, and NiCuMoO nanoparticles were successfully synthesized by sol–gel and ultra-sonication routes. The XRD, FTIR, Raman, EDX confirmed the structural formation. The lower energy bandgap of NiCuMoO/rGO nanocomposite makes it an efficient photocatalyst under sunlight. The NiCuMoO/rGO nanocomposite has superior photodecomposition activities for MB (99.2%,  $0.0523 \text{ min}^{-1}$ ) higher than others. The boosted absorption ability and enhanced  $e^-/h^+$  segregation results from integrating rGO with NiCuMoO improved the sunlight harvesting ability which ultimately increase degradation efficiency. From the scavenger experiment,  $HO^*$  and  $O_2^{*-}$  were found active for the photodecomposition of MB with suppressing efficiency of 55.0% and 45.0%. Moreover, only 6% photodecomposition efficiency was minimized after successive 6 runs. These



**Scheme 1** Photodegradation mechanism

findings encourage the synthesis of rGO-based nanocomposites for destructing toxin dyes in the future.

**Data availability** Data will be available on request.

## Declarations

**Conflict of interest** The authors declare that they have no known competing financial interests or personal relationships that could have appeared to influence the work reported in this paper.

## References

- Abbas H, Nadeem K, Hassan A et al (2020) Enhanced photocatalytic activity of ferromagnetic Fe-doped NiO nanoparticles. *Optik (stuttg)* 202:1–8. <https://doi.org/10.1016/j.ijleo.2019.163637>
- Agarwal V, Zetterlund PB (2021) Strategies for reduction of graphene oxide—a comprehensive review. *Chem Eng J* 405:127018. <https://doi.org/10.1016/j.cej.2020.127018>
- Ahuja P, Ujjain SK, Arora I, Samim M (2018) Hierarchically grown NiO-decorated polyaniline-reduced graphene oxide composite for ultrafast sunlight-driven photocatalysis. *ACS Omega* 3:7846–7855. <https://doi.org/10.1021/acsomega.8b00765>
- Ajeesha T, George M et al (2021) Nickel substituted  $MgFe_2O_4$  nanoparticles via co-precipitation method for photocatalytic applications. *Phys B Condens Matter* 606:412660. <https://doi.org/10.1016/j.physb.2020.412660>
- Alemán-Vázquez LO, Torres-García E, Villagómez-Ibarra JR, Cano-Domínguez JL (2005) Effect of the particle size on the activity of  $MoOxCy$  catalysts for the isomerization of heptane. *Catal Lett* 100:219–226. <https://doi.org/10.1007/s10562-004-3459-0>
- Al-Tohamy R, Ali SS, Li F et al (2022) A critical review on the treatment of dye-containing wastewater: ecotoxicological and health concerns of textile dyes and possible remediation approaches for environmental safety. *Ecotoxicol Environ Saf* 231:113160. <https://doi.org/10.1016/j.ecoenv.2021.113160>
- Areeb A, Yousaf T, Murtaza M, et al (2021) Green photocatalyst Cu/NiO doped zirconia for the removal of environmental pollutants. *Mater Today Commun* 28:102678. <https://doi.org/10.1016/j.mtcomm.2021.102678>
- Ata S, Shaheen I, Majid F et al (2021) Hydrothermal route for the synthesis of manganese ferrite nanoparticles and photocatalytic activity evaluation for the degradation of methylene blue dye. *Zeitschrift Fur Phys Chemie* 235:1433–1445. <https://doi.org/10.1515/zpch-19-1381>
- Bashir B, Khalid MU, Aadil M et al (2021)  $Cu_xNi_{1-x}O$  nanostructures and their nanocomposites with reduced graphene oxide: Synthesis, characterization, and photocatalytic applications. *Ceram Int* 47:3603–3613. <https://doi.org/10.1016/j.ceramint.2020.09.209>
- Bashir S, Habib A, Jamil A et al (2022) Fabrication of Ag-doped  $MoO_3$  and its nanohybrid with a two-dimensional carbonaceous material to enhance photocatalytic activity. *Adv Powder Technol* 33:103482. <https://doi.org/10.1016/j.apt.2022.103482>
- Bekena FT, Kuo DH, Kebede WL (2020) Universal and highly efficient degradation performance of novel  $Bi_2(O, S)_3/Mo(O, S)_2$  nanocomposite photocatalyst under visible light. *Sep Purif Technol* 247:117042. <https://doi.org/10.1016/j.seppur.2020.117042>
- Belkhaoui C, Mzabi N, Smaoui H, Daniel P (2019) Enhancing the structural, optical and electrical properties of ZnO nanopowders through (Al + Mn) doping. *Results Phys* 12:1686–1696. <https://doi.org/10.1016/j.rinp.2019.01.085>
- Bibi I, Muneer M, Iqbal M et al (2021) Effect of doping on dielectric and optical properties of barium hexaferrite: photocatalytic performance under solar light irradiation. *Ceram Int* 47:31518–31526. <https://doi.org/10.1016/j.ceramint.2021.08.030>
- Bodade AB, Taiwade MA, Chaudhari GN (2017) Bioelectrode based chitosan-nano copper oxide for application to lipase biosensor. *J Appl Pharm Res* 5:30–39

- Brijesh K, Nagaraja HS (2019) Lower band gap Sb/ZnWO<sub>4</sub>/r-GO nanocomposite based supercapacitor electrodes. *J Electron Mater* 48:4188–4195. <https://doi.org/10.1007/s11664-019-07185-8>
- Chandekar KV, Shkir M, Khan A et al (2021) Significant and systematic impact of yttrium doping on physical properties of nickel oxide nanoparticles for optoelectronics applications. *J Mater Res Technol* 15:2584–2600. <https://doi.org/10.1016/j.jmrt.2021.09.072>
- Dalrymple OK, Stefanakos E, Trotz MA, Goswami DY (2010) A review of the mechanisms and modeling of photocatalytic disinfection. *Appl Catal B Environ* 98:27–38. <https://doi.org/10.1016/j.apcatb.2010.05.001>
- Dharmaraj N, Prabu P, Nagarajan S et al (2006) Synthesis of nickel oxide nanoparticles using nickel acetate and poly(vinyl acetate) precursor. *Mater Sci Eng B* 128:111–114. <https://doi.org/10.1016/j.mseb.2005.11.021>
- Ehrampoush MH, Moussavi GHR, Ghaneian MT et al (2010) Removal of Methylene blue (MB) dye from textile synthetic wastewater using TiO<sub>2</sub>/UV-C photocatalytic process. *Aust J Basic Appl Sci* 4:4279–4285
- Fuku X, Matinise N, Masikini M et al (2018) An electrochemically active green synthesized polycrystalline NiO/MgO catalyst: Use in photo-catalytic applications. *Mater Res Bull* 97:457–465. <https://doi.org/10.1016/j.materresbull.2017.09.022>
- Gautam S, Agrawal H, Thakur M et al (2020) Metal oxides and metal organic frameworks for the photocatalytic degradation: a review. *J Environ Chem Eng* 8:103726. <https://doi.org/10.1016/j.jece.2020.103726>
- Gawali SR (2020) Synthesis and characterization of samarium doped nio nanoparticles. *Int J Sci Technol Res* 9:2960–2964
- Ghafoor A, Bibi I, Ata S et al (2021) Synthesis and characterization of magnetically separable La<sub>1-x</sub>Bi<sub>x</sub>Cr<sub>1-y</sub>Fe<sub>y</sub>O<sub>3</sub> and photocatalytic activity evaluation under visible light. *Zeitschrift Fur Phys Chemie* 235:1413–1431. <https://doi.org/10.1515/zpch-2020-1747>
- Ghosh MP, Datta S, Sharma R et al (2021) Copper doped nickel ferrite nanoparticles: Jahn-Teller distortion and its effect on microstructural, magnetic and electronic properties. *Mater Sci Eng B Solid-State Mater Adv Technol* 263:114864. <https://doi.org/10.1016/j.mseb.2020.114864>
- Gusain R, Gupta K, Joshi P, Khatri OP (2019) Adsorptive removal and photocatalytic degradation of organic pollutants using metal oxides and their composites: a comprehensive review. *Adv Colloid Interface Sci* 272:102009. <https://doi.org/10.1016/j.cis.2019.102009>
- Hakimyfarid A, Zalpour N, Zarinabadi F (2022) Physical properties and photocatalytic activity of new classes of Mx-ZnO-Bi<sub>2</sub>O<sub>3</sub>-WO<sub>3</sub> and Mx-ZnO-Bi<sub>2</sub>O<sub>3</sub>-MoO<sub>2</sub> (M = None, Fe Co, and Ni) nanocomposites. *J Aust Ceram Soc* 58:817–830. <https://doi.org/10.1007/s41779-022-00727-0>
- Hannachi E, Slimani Y, Nawaz M et al (2022a) Synthesis, characterization, and evaluation of the photocatalytic properties of zinc oxide co-doped with lanthanides elements. *J Phys Chem Solids* 170:110910. <https://doi.org/10.1016/j.jpcs.2022.110910>
- Hannachi E, Slimani Y, Nawaz M et al (2022b) Preparation of cerium and yttrium doped ZnO nanoparticles and tracking their structural, optical, and photocatalytic performances. *J Rare Earths*. <https://doi.org/10.1016/j.jre.2022.03.020>
- Iqbal S, Bibi I, Ata S et al (2020) Gd and Co-substituted LaNiO<sub>3</sub> and their nanocomposites with r-GO for photocatalytic applications. *Diam Relat Mater* 110:108119. <https://doi.org/10.1016/j.diamond.2020.108119>
- Jiao Y, Liu Y, Qu F et al (2015) Visible-light-driven photocatalytic properties of simply synthesized α-Iron(III)oxide nanourchins. *J Colloid Interface Sci* 451:93–100. <https://doi.org/10.1016/j.jcis.2015.03.055>
- Kanjwal MA, Chronakis IS, Barakat NAM (2015) Electrospun NiO, ZnO and composite NiO–ZnO nanofibers/photocatalytic degradation of dairy effluent. *Ceram Int* 41:12229–12236. <https://doi.org/10.1016/j.ceramint.2015.06.045>
- Kannan K, Radhika D, Reddy KR et al (2021) Gd<sup>3+</sup> and Y<sup>3+</sup> co-doped mixed metal oxide nanohybrids for photocatalytic and antibacterial applications. *Nano Express*. <https://doi.org/10.1088/2632-959X/abdd87>
- Kate RS, Bulakhe SC, Deokate RJ (2019) Co doping effect on structural and optical properties of nickel oxide (NiO) thin films via spray pyrolysis. *Opt Quantum Electron* 51:1–19. <https://doi.org/10.1007/s11082-019-2026-2>
- Kavitha C (2022) A review on reduced graphene oxide hybrid nano composites and their prominent applications. *Mater Today Proc* 49:811–816. <https://doi.org/10.1016/j.matpr.2021.05.343>
- Khatri A, Rana PS (2020) Visible light assisted photocatalysis of methylene blue and rose bengal dyes by iron doped NiO nanoparticles prepared via chemical co-precipitation. *Phys B Condens Matter*. <https://doi.org/10.1016/j.physb.2019.411905>
- Lakshmana Reddy N, Rao VN, Kumari MM et al (2018) Effective shuttling of photoexcitons on CdS/NiO core/shell photocatalysts for enhanced photocatalytic hydrogen production. *Mater Res Bull* 101:223–231. <https://doi.org/10.1016/j.materresbull.2018.01.043>
- Lingaraju K, Raja Naika H, Nagaraju G, Nagabhushana H (2019) Biocompatible synthesis of reduced graphene oxide from *Euphorbia heterophylla* (L.) and their in-vitro cytotoxicity against human cancer cell lines. *Biotechnol Rep* 24:e00376. <https://doi.org/10.1016/j.btre.2019.e00376>
- Liu L, Hu N, An Y et al (2020) Ag<sub>2</sub>O and NiO decorated CuFe<sub>2</sub>O<sub>4</sub> with enhanced photocatalytic performance to improve the degradation efficiency of methylene blue. *Materials (basel)* 13:4760. <https://doi.org/10.3390/ma13214760>
- Maniammal K, Madhu G, Biju V (2018) Nanostructured mesoporous NiO as an efficient photocatalyst for degradation of methylene blue: structure, properties and performance. *Nano-Struct Nano-Objects* 16:266–275. <https://doi.org/10.1016/j.nanoso.2018.07.007>
- Marinoiu A, Raceanu M, Andrulevicius M et al (2020) Low-cost preparation method of well dispersed gold nanoparticles on reduced graphene oxide and electrocatalytic stability in PEM fuel cell. *Arab J Chem* 13:3585–3600. <https://doi.org/10.1016/j.arabjc.2018.12.009>
- Munawar T, Mukhtar F, Nadeem MS et al (2020a) Novel direct dual-Z-scheme ZnO-Er<sub>2</sub>O<sub>3</sub>-Nd<sub>2</sub>O<sub>3</sub>@reduced graphene oxide heterostructured nanocomposite: Synthesis, characterization and superior antibacterial and photocatalytic activity. *Mater Chem Phys*. <https://doi.org/10.1016/j.matchemphys.2020.123249>
- Munawar T, Mukhtar F, Nadeem MS et al (2020b) Structural, optical, electrical, and morphological studies of rGO anchored direct dual-Z-scheme ZnO-Sm<sub>2</sub>O<sub>3</sub>-Y<sub>2</sub>O<sub>3</sub> heterostructured nanocomposite: an efficient photocatalyst under sunlight. *Solid State Sci*. <https://doi.org/10.1016/j.solidstatesciences.2020.106307>
- Munawar T, Yasmeen S, Mukhtar F et al (2020c) Zn<sub>0.9</sub>Ce<sub>0.05</sub>M<sub>0.05</sub>O (M = Er, Y, V) nanocrystals: structural and energy bandgap engineering of ZnO for enhancing photocatalytic and antibacterial activity. *Ceram Int* 46:14369–14383. <https://doi.org/10.1016/j.ceramint.2020.02.232>
- Munawar T, Mukhtar F, Nadeem MS et al (2022) Fabrication of dual Z-scheme TiO<sub>2</sub>-WO<sub>3</sub>-CeO<sub>2</sub> heterostructured nanocomposite with enhanced photocatalysis, antibacterial, and electrochemical performance. *J Alloys Compd* 898:162779. <https://doi.org/10.1016/j.jallcom.2021.162779>
- Nath A, Shah A, Singh LR, Mahato M (2021) Waste plastic-derived NiO-MWCNT composite as visible light photocatalyst for degradation of methylene blue dye. *Nanotechnol Environ Eng* 6:1–14. <https://doi.org/10.1007/s41204-021-00163-8>

- Noreen S, Khalid K, Iqbal M et al (2021) Eco-benign approach to produce biodiesel from neem oil using heterogeneous nano-catalysts and process optimization. *Environ Technol Innov* 22:101430. <https://doi.org/10.1016/j.eti.2021.101430>
- Oladipo AA (2021) Rapid photocatalytic treatment of high-strength olive mill wastewater by sunlight and UV-induced  $\text{CuCr}_2\text{O}_4/\text{CaFe-LDO}$ . *J Water Process Eng* 40:101932. <https://doi.org/10.1016/j.jwpe.2021.101932>
- Papadimitropoulos G, Vourdas N, Vamvakas VE, Davazoglou D (2006) Optical and structural properties of copper oxide thin films grown by oxidation of metal layers. *Thin Solid Films* 515:2428–2432. <https://doi.org/10.1016/j.tsf.2006.06.002>
- Parashar M, Shukla VK, Singh R (2020) Metal oxides nanoparticles via sol–gel method: a review on synthesis, characterization and applications. *J Mater Sci Mater Electron* 31:3729–3749. <https://doi.org/10.1007/s10854-020-02994-8>
- Patel KN, Deshpande MP, Chauhan K et al (2017) Synthesis, structural and photoluminescence properties of nano-crystalline Cu doped NiO. *Mater Res Express* 4:105027. <https://doi.org/10.1088/2053-1591/aa90ad>
- Pirzada BM, Mehraj O, Bhat SA, Sabir S (2018) Efficient visible-light-driven photocatalytic activity and enhanced charge transfer properties over Mo-doped  $\text{WO}_3/\text{TiO}_2$  nanocomposites. *J Environ Chem Eng* 6:3204–3212. <https://doi.org/10.1016/j.jece.2018.05.004>
- Qi K, Cheng B, Yu J, Ho W (2017) Review on the improvement of the photocatalytic and antibacterial activities of ZnO. *J Alloys Compd* 727:792–820. <https://doi.org/10.1016/j.jallcom.2017.08.142>
- Ramya S, Viruthagiri G, Gobi R et al (2016) Synthesis and characterization of  $\text{Ni}^{2+}$  ions incorporated CuO nanoparticles and its application in antibacterial activity. *J Mater Sci Mater Electron* 27:2701–2711. <https://doi.org/10.1007/s10854-015-4080-2>
- Santhosh K, Chouti S et al (2021) Tailoring hierarchical porous  $\text{TiO}_2$  based ternary rGO/NiO/ $\text{TiO}_2$  photocatalyst for efficient hydrogen production and degradation of Rhodamine B. *J Mol Struct* 1235:130222. <https://doi.org/10.1016/j.molstruc.2021.130222>
- Senobari S, Nezamzadeh-Ejhi A (2018) A comprehensive study on the enhanced photocatalytic activity of CuO–NiO nanoparticles: designing the experiments. *J Mol Liq* 261:208–217. <https://doi.org/10.1016/j.molliq.2018.04.028>
- Shakil M, Inayat U, Tanveer M et al (2022) NiO and Ag–Cd co-doped NiO nanoparticles: study of photocatalytic degradation of rhodamine B dye for wastewater treatment. *Int J Environ Sci Technol*. <https://doi.org/10.1007/s13762-022-04101-2>
- Shiri HM, Ehsani A, Behjatmanesh-Ardakani R, Hajghani S (2019) Electrosynthesis of  $\text{Y}_2\text{O}_3$  nanoparticles and its nanocomposite with POAP as high efficient electrode materials in energy storage device: surface, density of state and electrochemical investigation. *Solid State Ionics* 338:87–95. <https://doi.org/10.1016/j.ssi.2019.05.008>
- Shkir M, Palanivel B, Khan A et al (2021) Tailoring the structural, optical and remarkably enhanced photocatalytic activities of nickel oxide nanostructures through cobalt doping. *Surf Interfaces*. <https://doi.org/10.1016/j.surfin.2021.101515>
- Shu H, Xie J, Xu H et al (2010) Structural characterization and photocatalytic activity of NiO/AgNbO<sub>3</sub>. *J Alloys Compd* 496:633–637. <https://doi.org/10.1016/j.jallcom.2010.02.148>
- Singh A, Goyal V, Singh J et al (2022) Structurally and morphologically engineered single-pot biogenic synthesis of NiO nanoparticles with enhanced photocatalytic and antimicrobial activities. *J Clean Prod* 343:131026. <https://doi.org/10.1016/j.jclepro.2022.131026>
- Slimani Y, Hannachi E (2021) 16-Ru-based perovskites/RGO composites for applications in high performance supercapacitors. In: Khan I, Khan A, Khan MMA et al (eds) Woodhead publishing series in composites science and engineering. Woodhead Publishing, pp 335–354
- Sone BT, Fuku XG, Maaza M (2016) Physical and electrochemical properties of green synthesized bunsenite NiO nanoparticles via Callistemon Viminalis' extracts. *Int J Electrochem Sci* 11:8204–8220. <https://doi.org/10.20964/2016.10.17>
- Song L, Zhang S (2010) A simple mechanical mixing method for preparation of visible-light-sensitive NiO–CaO composite photocatalysts with high photocatalytic activity. *J Hazard Mater* 174:563–566. <https://doi.org/10.1016/j.jhazmat.2009.09.088>
- Tabish M, Malik MU, Khan MA et al (2021) Construction of NiCo/graphene nanocomposite coating with bulges-like morphology for enhanced mechanical properties and corrosion resistance performance. *J Alloys Compd* 867:159138. <https://doi.org/10.1016/j.jallcom.2021.159138>
- Tadjarodi A, Pradehkorram R, Imani M, et al (2014) A simplified microwave-assisted synthesis of NiMoO<sub>4</sub> nanoparticles by using organic driving agent and study of photocatalytic activity. *c008*. <https://doi.org/10.3390/ecsoc-18-c008>
- Taeño M, Maestre D, Ramírez-Castellanos J et al (2021) Towards control of the size, composition and surface area of nio nanostructures by sn doping. *Nanomaterials* 11:1–13. <https://doi.org/10.3390/nano11020444>
- Takanabe K (2017) Photocatalytic water splitting: quantitative approaches toward photocatalyst by design. *ACS Catal* 7:8006–8022. <https://doi.org/10.1021/acscatal.7b02662>
- Theerthagiri J, Chandrasekaran S, Salla S et al (2018) Recent developments of metal oxide based heterostructures for photocatalytic applications towards environmental remediation. *J Solid State Chem* 267:35–52. <https://doi.org/10.1016/j.jssc.2018.08.006>
- Varunkumar K, Hussain R, Hegde G, Ethiraj AS (2017) Effect of calcination temperature on Cu doped NiO nanoparticles prepared via wet-chemical method: structural, optical and morphological studies. *Mater Sci Semicond Process* 66:149–156. <https://doi.org/10.1016/j.mssp.2017.04.009>
- Yadav S, Rani N, Saini K (2022) Synthesis and characterization of NiO/Cr<sub>2</sub>O<sub>3</sub> nanocomposite with effective sunlight driven photocatalytic degradation of organic dyes. *Environ Sci Pollut Res*. <https://doi.org/10.1007/s11356-022-22746-x>
- Yang X, Wang D (2018) Photocatalysis: from fundamental principles to materials and applications. *ACS Appl Energy Mater* 1:6657–6693. <https://doi.org/10.1021/acsaem.8b01345>
- Yaseen DA, Scholz M (2019) Textile dye wastewater characteristics and constituents of synthetic effluents: a critical review. Springer, Berlin Heidelberg
- Yasin G, Anjum MJ, Malik MU et al (2020a) Revealing the erosion-corrosion performance of sphere-shaped morphology of nickel matrix nanocomposite strengthened with reduced graphene oxide nanoplatelets. *Diam Relat Mater* 104:107763. <https://doi.org/10.1016/j.diamond.2020.107763>
- Yasin G, Arif M, Mehtab T et al (2020b) A novel strategy for the synthesis of hard carbon spheres encapsulated with graphene networks as a low-cost and large-scalable anode material for fast sodium storage with an ultralong cycle life. *Inorg Chem Front* 7:402–410. <https://doi.org/10.1039/c9qi01105f>
- You J, Guo Y, Guo R, Liu X (2019) A review of visible light-active photocatalysts for water disinfection: features and prospects. *Chem Eng J* 373:624–641. <https://doi.org/10.1016/j.cej.2019.05.071>
- Zaharia C, Suteu D, Muresan A, et al (2009) Textile wastewater treatment by homogeneous oxidation with hydrogen peroxide. *Environ Eng Manag J* 8:1359–1369. <https://doi.org/10.30638/eejm.2009.199>
- Zaharia C, Suteu D (2016) Textile organic dyes—characteristics, polluting effects and separation/elimination procedures from industrial effluents—a critical overview. *Org Pollut Ten Years after Stock Conv Environ Anal Updat* 3:55–86



- Zhang L, Jaroniec M (2018) Toward designing semiconductor-semiconductor heterojunctions for photocatalytic applications. *Appl Surf Sci* 430:2–17. <https://doi.org/10.1016/j.apsusc.2017.07.192>
- Zhu Q, Liu N, Zhang N et al (2018) Efficient photocatalytic removal of RhB, MO and MB dyes by optimized Ni/NiO/TiO<sub>2</sub> composite thin films under solar light irradiation. *J Environ Chem Eng* 6:2724–2732. <https://doi.org/10.1016/j.jece.2018.04.017>

**Publisher's Note** Springer Nature remains neutral with regard to jurisdictional claims in published maps and institutional affiliations.

Springer Nature or its licensor (e.g. a society or other partner) holds exclusive rights to this article under a publishing agreement with the author(s) or other rightsholder(s); author self-archiving of the accepted manuscript version of this article is solely governed by the terms of such publishing agreement and applicable law.